Ultrahigh Performance Nanoengineered Graphene-Concrete Composites for Multifunctional Applications

Dimitar Dimov, Iddo Amit, Olivier Gorrie, Matthew D. Barnes, Nicola J. Townsend, Ana I. S. Neves, Freddie Withers, Saverio Russo, and Monica Felicia Craciun*
Centre for Graphene Science, College of Engineering, Mathematics and Physical Sciences, University of Exeter, Exeter EX4 4QF, UK

There is a constant drive for development of ultrahigh performance multifunctional construction materials by the modern civil engineering technologies. These materials have to exhibit enhanced performance in terms of durability and mechanical strength, and incorporate functionalities that satisfy multiple uses in order to be suitable for future emerging structural applications. To address these challenges, there is a wide consensus in the research community that concrete, the most used composite construction material worldwide, has to be engineered at the nanoscale, where its chemical and physico-mechanical properties can be truly enhanced. Here we report an innovative multifunctional nanoengineered concrete composite displaying an unprecedented range of enhanced properties compared to standard concrete. These include an increase of up to 146% in the compressive strength and up to 79.5% in the flexural one while at the same time we find an enhanced electrical and thermal performance. A surprising decrease in water permeability by nearly 400% compared to the standard concrete makes this novel composite material ideally suitable for constructions in areas subject to flooding. The unprecedented gamut of functionalities that we report in this paper are produced by the addition of water-stabilised graphene dispersions, an advancement in the emerging field of nanoengineered concrete which can be readily applied in a more sustainable, environmentally-friendly construction industry.

INTRODUCTION

The new global standards of modern civil technologies, continuously requiring more demanding infrastructure, are driving the development of ultra-high-performance multifunctional construction materials. In particular, extensive efforts are focused on increasing the performance and functionality of concrete, the most used construction material worldwide. A truly step changing approach to enhance mechanical performance and to provide novel functionalities requires intervention at the nano-scale since most of the damage caused to concrete can be traced back to chemical and mechanical defects in the cement structure. Current research efforts are therefore directed at exploring new ways of enhancing the performance of concrete by nano-engineering the chemical and physico-mechanical properties of cement, the main binding element in the composition of concrete. The cement particles, which consist of a variety of chemical elements (such as calcium silicates, aluminates and aluminoferrites) undergo transformation from powder form to fibrous crystals upon reacting with water, known as the hydration reaction[1]. Their growth and mechanical interlocking over time are the most significant factor in shaping the material properties of concrete. The outstanding chemical and physical properties of nanomaterials provide the most efficient enhancement for the internal matrix of concrete, and recent progress in nano-modification of cement composite materials has enabled applications in structural reinforcement, reduction of environmental pollution[2] and production of self-cleaning materials[3].

Previous studies[4–7,30–32] have largely focused on the incorporation of nanomaterials in cement. These include the incorporation of carbon nanotubes (CNT)[7] and graphene oxide (GO)[4,5] in cement which resulted in a 50% (for CNT) and 33% (for GO) improvement of the compressive strength, while industrial grade thin graphite platelets (100nm thickness)[6] were shown to improve the thermal conductivity. However, these findings do not extend directly to concrete, as the addition of sand and aggregate changes the physico-mechanical behaviour of the material. Moreover, to date the role of atomically thin materials on nano-engineering of concrete is yet to be explored and this holds the promise to change the landscape of construction materials leading to a more sustainable urbanization with lower carbon foot print and more resilient constructions against natural disasters.

Here we report innovative few-atoms-thin graphene enabled nano-engineered multifunctional concrete composites which display an unprecedented range of enhanced properties compared to standard concrete. We demonstrate an extraordinary increase of up to 146% in the compressive strength, up to 79.5% in the flexural one and a decrease in the maximum displacement due to compressive loading by 78%. At the same time we find an enhanced electrical and thermal performance with 88% increase in heat capacity. A remarkable decrease in water permeability by nearly 400% compared to the standard concrete, that is an extremely sought after property for long durability of concrete structures, makes this novel composite material ideally suitable for constructions in areas subject to flooding. Finally, we show that the inclusion of graphene in nowadays concrete would lead to a reduction by 50% of the required concrete material while still fulfilling the specifications for the loading of buildings. This would lead to a significant reduction of 446kg/tonne of the carbon emissions by the cement manufacturing. Crucially, we demonstrate that the unprecedented gamut of functionalities that we report in this

paper are produced by the addition of water-stabilised graphene dispersions, with high yield, low cost and compatible with the large scale manufacturing required for the use of this material in practical applications. The unprecedented range of functionalities and properties uncovered in our study represents an advancement in the emerging field of nanoengineered materials which can be readily applied in a more sustainable, environmentally-friendly construction industry.

RESULTS

Fabrication of water dispersed graphene

Since the isolation of graphene, various methods for large scale production were demonstrated including Chemical Vapor Deposition[8], chemical exfoliation[9] and liquid phase exfoliation[10–13]. The latter allows the separation of graphite into graphene layers in a liquid medium to produce few-layer graphene dispersions, stabilised by a surfactant[10–12] or solvents[13]. Recent progress in liquid phase exfoliation made by using high-shear blending[12] has significantly improved the quality of graphene and the volume–time dependency of exfoliating graphene in water, allowing for production of more than 100 litres per hour of defect-free graphene solution[12]. In this work we demonstrate that the high-shear exfoliation of graphene in water is extremely efficient for the fabrication of graphene reinforced concrete as it can substitute water directly in the concrete mixture and it is industrially scalable. We use two types of graphene materials, surfactant functionalised graphene and commercially-available graphene nanoplatelets, both dispersed in water using high-shear blending.

To introduce multifunctionalities to concrete using graphene, we first prepared suspensions of graphene in water by high-shear liquid phase exfoliation of graphite powder using the surfactant sodium cholate (see Fig. 1A), resulting in surfactant functionalised graphene (FG). Fig. 1B shows the high-shear mixer used in this work. The exfoliation process occurs inside the square hole head, shown in the inset of Fig. 1B, where the rotor blade shears platelets at very high speed (up to 8000 rpm) against the square hole head. When graphite flakes are trapped in the narrow space between the rotor and the head, shear forces developed in the liquid separate the weakly (van der Waals) coupled graphene layers of graphite. The resulting suspension of exfoliated graphene flakes dispersed in water is shown in Fig. 1C, with the schematic structure of FG illustrated in the inset of Fig. 1C. As it has previously been demonstrated, the surfactant can play multiple roles in the preparation of water suspended graphene, i.e. it helps decrease the water surface tension to match that of graphene and make the exfoliation feasible, allows the formation of uniform mixtures of graphite precursor, and most importantly stabilises the exfoliated graphene nanosheets and prevents them from aggregating[10,11]. Suspensions with various concentrations of FG in water were prepared (see Supplementary Materials (SM) Fig. S1.) and used for concrete mixing. We have also investigated the incorporation in concrete of ultra thin graphite (UTGr) flakes prepared by the same method as FG in order to establish whether graphene or graphite is the most efficient nanoreinforcement for concrete. Finally we have incorporated in the concrete commercially available graphene nanoplatelets of industrial grade (IG), by dispersing dried powder in water using the high-shear mixer shown in Fig. 1C.

Prior to their incorporation in concrete we have characterised graphene (FG and IG) and graphite (UTGr) materials by fabricating thin films which were investigated by optical and scanning electron microscopy (SEM), as well as Raman spectroscopy to determine the number of layers and level of defects. To this end, after decanting the suspension and discarding the heavy excess graphite, the dispersion was filtered through a mixed cellulose hydrophilic Millipore(R) membrane with 0.025 μm pore size. Fig. 1D shows a continuous film of FG on the filter membrane. The FG was then released from the filter by immersion and floating in water as shown in Fig. 1D and transferred onto a SiO_2 substrate (see SM Fig. S1.). SEM analysis revealed that the film consists of flakes with sizes ranging from 0.07 μm^2 up to 1.06 μm^2 in area (for details see SM Fig. S3.).

Scanning Raman spectroscopy was performed on representative areas of 20×20 μm^2 and used to study the number of layers and the nature of defects in the continuous film. Fig. 1E shows single scans of the 2D peak for FG, UTGr, IG and bulk graphite. We have estimated the number of layers from the 2D peak shift in graphene relative to graphite, using the method developed by Paton *et al.* for graphene films obtained from dispersions[12](see SM for details). We found that FG graphene consists of flakes with the number of layers that varies from 4 to 7 with the majority of flakes 6 graphene layers thick (see the map on Fig. 1F). IG graphene consists of flakes with number of layers varying between 10 and 14 with the majority of the flakes containing 10 to 11 graphene layers (see the map on Fig. 1F). UTGr consists of flakes with the majority of 20 to 21 layers.

To assess the level of defects we have measured the D peak (around 1340cm^{-1}), the G peak (around 1600cm^{-1}) and D' peak which is visible as a small shoulder on the right side of G. The intensity ratio of D and G peaks I_D/I_G which is one of the parameters used to quantify the defects in graphene varies between the three different types of graphene. We have studied the range of intensity ratios for UTGr, IG and FG using Raman maps as shown on Fig. 1G, showing that defects are present everywhere. We selected one representative scan of each map corresponding to the intensity ratio with highest occurrence (0.08 for UTGr, 0.7 for IG and 0.53 for FG) and plotted the single scan, focusing on D, G and D' peaks as shown on Fig. 1H. The relationship between the I_D/I_G and $I_D/I_{D'}$ ratios is an effective tool to quantify the nature of defects. Specifically, a ratio around 14 corresponds to sp^3 defects, whereas $I_D/I_{D'}$ of 7 and 3.5 correspond to vacancy and boundary defects, respectively[14]. As shown in Fig. 1I, the $I_D/I_{D'}$ of ≈ 2.39

found in our graphene films demonstrates that for the whole range of I_D/I_G the level of defects is always below the benchmark for boundary defects. Therefore we can conclude that the shear mixing does not introduce defects to the basal plane of exfoliated graphene.

Strength of graphene nanoengineered concrete

The high-shear liquid phase exfoliation method used to manufacture water-based graphene dispersions is suitable for combining graphene with concrete because of the potential for high throughput of the industrial scale equivalent equipment, i.e. in excess of 100 litres per hour. Thus we have incorporated graphene into concrete by mixing the water-based graphene dispersions with Ordinary Portland cement (OPC), fine dry sand and $10mm$ coarse aggregate, see Fig. 2A and Methods. Various solutions with different concentrations of FG and IG in water were investigated in order to optimize the performance of the graphene reinforced concrete. Subsequently, cubes of concrete as shown in Fig. 2B were prepared, cured and tested for their compressive strength according to standards regulating the architectural and engineering designs (see S7 in SM). Specifically, the fresh concrete mix was poured in standard 10x10x10 cm steel moulds, removed after 24 hours and kept in a water tank to cure (see Methods and SM for more details). One of the key mechanical properties of concrete is the evolution of compressive strength over time. Therefore, we have tested the cubes after intervals of curing time ranging between 7 to 28 days, in order to extract the early age and later age strength values. The graphene reinforced concrete samples were compared with standard concrete. To this end a control sample group was produced following the same procedure, but with replacing the graphene water solution with tap water. These measurements ensure that the concrete samples investigated in this work comply with the test batches used for casting at construction sites that are prepared in accordance with engineering designs.

The uniaxial compressive and flexural strength tests on concrete cubes and beams, respectively, are the most widely used methods for evaluating the fundamental mechanical properties of concrete. Therefore below we will focus on these type of measurements to characterize the mechanical properties of graphene reinforced concrete and evaluate the effectiveness of this type of reinforcement. The compressive stress was determined by dividing the measured applied force by the area of the cube. The strain was obtained from standard mechanical strain gauge. Fig. 2C shows typical stress–strain curves that we measured under compressive loading for concrete cubes cured for 7 days and produced using the three different types of concrete: concrete reinforced with IG, FG and UTGr as well as standard water based concrete. The stress-strain curve consists of two parts, i.e. the ascending branch (from 0 to the maximum strength) and the descending branch (from maximum strength to the failure point). The first half of the ascending branch is approximately a straight line and corresponds to the elastic region. This segment is labeled as 0.5 f_c, with f_c being the maximum strength of the cube. In this region the deformations due to compressive loading are reversible and mainly caused by slipping between bulk aggregates and cement crystals. The slope of this section gives the Young's modulus (E_c) of the material, which is a measure of its stiffness. As it can be seen from Fig. 2C, graphene reinforcement results in a steeper elastic region compared to standard concrete, indicating a stiffer material with stronger bonds between cement and aggregates. On the other hand, the reinforcement with ultra thin graphite leads to decrease in the performance, with lowering of the overall strength, while E_c remains relatively unchanged. This finding suggests that the 24nm thick graphite particles are hampering the hydration reaction and are blocking the cement crystals form proper interlocking. Fig. 2D shows the extracted values for E_c as a function of curing time. We observed that for early age concrete samples (i.e. after 7 days of curing) both FG and IG reinforced concrete have higher E_c than standard concrete – 30.7% and 35.8% increase respectively whereas graphite reinforcement leaves the E_c unchanged. Furthermore, the values measured for later age concrete (i.e. after 28 days of curing) are very similar both in number and percentage increase to the values observed after 7 days of curing. This suggests that durability of the concrete remains stable over time, making it suitable for industrial applications.

Upon increasing the stress above the elastic region, a gradual decrease in the slope of the stress–strain curve is observed. This is the plastic deformation region where the bonds between cement and aggregates still undergo a period of strain hardening, but with non-reversible changes. These effects are due to the viscous flow of hydrated cement paste in concrete, as well as to the propagation and growth of initial micro-cracks[15]. Also in this region we observe a similar behaviour to the elastic region, where graphene reinforced concrete is stiffer than standard concrete. When the stress is increased closer to the peak point in the stress–strain curve, internal cracks speed their propagation, and the specimen is about to fail. In Fig. 2D it is evident that f_c of graphene reinforced concrete has higher values than standard concrete whereas graphite reinforcement lowers the f_c of standard concrete. Fig. 2E is a plot of f_c as a function of curing time, where each data point is an average of 3 cubes. 7 days after curing an 18.6% increase in strength is observed for FG reinforcement and 14.3% increase with IG reinforcement, compared to the standard concrete. To further investigate how f_c of concrete evolves with varying concentration of graphene we have performed a systematic study of the stress-strain curve for a wide range of graphene concentrations. Fig. 2F and Fig. 2G show the evolution of E_c and f_c for IG. The optimal IG concentration was found to be 0.7 g/L and it increases both E_c and f_c by 80.5% and 146% respectively. similarly we found that for FG reinforcement the best performance is achieved for 0.59g/L concentration of FG (See SM).

These studies demonstrate that reinforcing concrete with graphene, for both types of materials, has significant impact on increasing the early age compressive strength of concrete. With increasing the curing time to 14, 21 and 28 days, the strength of all the samples continues to increase, with graphene reinforced concrete remaining stronger than standard concrete. In particular the testing performed after 28 days of curing reveals that reinforcement with IG results in about 26% stronger concrete than the standard concrete, demonstrating the possibility of later age reinforcement of concrete with graphene.

To further confirm that graphene reinforces concrete, we performed statistical studies by preparing and testing more than 150 concrete cubes. This included batches of 20 samples for each of the 3 experimental groups (Standard Concrete, 0.59g/L FG and 0.7g/L IG), all of them tested for compressive strength after 7 days and 28 days of curing. Fig. 3A and 3B show the statistical study of E_c, whereas Fig. 3C and 3D show the study of f_c, after curing for 7 and 28 days respectively. These studies confirm the measurements reported in Fig. 2D and Fig. 2E and support the conclusion that incorporation of graphene into the concrete matrix increases the compressive strength of both the early and later age concrete.

To better understand the internal deformations and dislocations between cement and aggregate. Cyclic loading compression tests, measuring the stress–strain curve for 5 loops of loading and unloading up to 60% of the f_c. Fig. 4A is a plot focusing on the maximum vertical displacement, measured directly from the mechanical strain gauge apparatus, of one sample after each cycle loading. Fig. 4A shows that even after multiple loading-deloading patterns the graphene reinforced samples do not experience as much internal deformation as standard concrete. As shown in Fig. 4B, the overall δ_{max} of the concrete decreases with increasing the concentration of graphene indicating stronger molecular bonds as concrete is being progressively reinforced. We then focus on the first loop of the F-δ plot to study the maximum plastic strain ε_{pl}. The method derived by Mander *et al.*[20] was used to calculate ε_{pl} – it lies on the secant line of the unloading curve (the black line) of the loop, as shown on Fig. 4C. The plastic strain indicates the residual deformation when the applied stresses are removed. As it can be seen from Fig. 4D, for the whole range of graphene concentrations the reinforcement helps to decrease the ε_{pl} when compared to standard concrete (i.e. C_{IG}=0) which is in agreement with overall increase in f_c and E_c.

After having established that graphene reinforcement increases the compressive strength of concrete, we now turn our attention to the study of flexural strength (f_{cr}) of graphene reinforced concrete. The most common method for testing and calculating f_{cr} is the 3-point bending test which is performed on rectangular beams with dimensions of 10x10x400 cm as shown on Fig. 5A. The force is applied at the centre of the beam which is resting on two supports at equal distance from the centre point. The mid-span deflection δ is measured using displacement transducer in order to give better understanding of the flexural modulus (E_{cr}). Beams were prepared for standard concrete and for different IG concentrations and tested after 7 and after 28 days of curing. Fig. 5B shows typical stress-strain curves extracted from the 3-point bending test after 7 days of specimen curing. The flexural strength is given by the maximum flexural stress. Similarly to the compressive modulus of elasticity the flexural one is also dependent on the slope of the tangent line of the first 50% of the curve, however it includes the second moment of area too (see SM for details).

Fig. 5C and Fig.5E show the E_{cr} and f_{cr} of standard concrete and IG reinforced concrete beams after 7 days of curing. Clearly as the graphene concentration is increased both properties are improved, showing maximum increase with IG concentration of 0.6g/L – 21.8% and 18.6% for E_{cr} and f_{cr} respectively. 28 days after specimen curing the mechanical improvement is still present with 78.5% increase in E_{cr} and 79% for f_{cr} as shown on Fig. 5D and F for the same IG concentration. This massive increase in flexural modulus and strength are in agreement with the increase of maximum f_c and decrease of compressive δ_{max} shown in previous figures.

As we will now discuss, the observed strengthening of concrete by incorporation of graphene can be interpreted in terms of the modification of cement hydration reaction. To understand the details of our discussion, it is important to recall some basic aspects of this reaction and relevant properties of graphene. Concrete is composed of fine and bulk aggregate, mechanically interlocked as a result of the hydration reaction between cement and water. Upon reacting with water molecules, the cement micro crystalline powder undergoes physical transformations to fibrous crystals containing mainly calcium silicates, alumino-ferrites and calcium hydroxide ($Ca(OH)_2$). More than 40 variations of silicate crystals have been reported to occur in the composition of cement[16] and they form the calcium silicate hydrate (C-S-H) gel, which is one of the main elements responsible for the mechanical properties of concrete. Graphene is a crystalline sheet of carbon atoms, packed in a hexagonal structure. Graphene monolayers and few-layers have a large specific surface area and high Youngs modulus (E_c around 2 TPa[17]). As it has already been demonstrated, graphene interacts with various elements forming the vast elements C-S-H groups[16] and alters the morphology of the hydration crystals[6]. In particular, due to the high surface energy of graphene, C-S-H particles bond to graphene and act as nucleation sites, promoting the growth of C-S-H gels along the graphene flakes. This process leads to an increase in the bond strength of cement[18]. As we have demonstrated in Fig. 3, the defects found in our graphene materials are only due to boundaries of the flakes. Therefore the defect–free basal plane of our graphene material forms an ideal platform for the growth of C-S-H crystals with higher degree of crystallinity than the crystals occurring in the standard concrete. The degree of crystallinity is one of the most important physical

parameters responsible for the mechanical properties of a material and determines various parameters, such as the Young modulus and strength. Furthermore, combining C-S-H which has an E_c of 23.8 GPa[19] with graphene (E_c of 2 TPa) would lead to a considerable increase in the E_c of the composite material. Therefore, we believe that the possible formation of C-S-H crystals along the graphene flakes with high degree of crystallinity combined with the high Youngs modulus of graphene could lead to a stiffer graphene–C-S-H composite material than C-S-H alone, as observed experimentally.

Another factor which determines the compressive strength of concrete is the degree of porosity, which results in empty voids within the cement paste due to unhydrated crystals or leaching of $Ca(OH)_2$. $Ca(OH)_2$ crystals tend to form on a nano-scale level and due to their high solubility, leach out when concrete is exposed to fresh water. This process increases the porosity of concrete and therefore, decreases its strength. We believe that graphene reinforcement could also have an effect on decreasing the degree of porosity. Indeed previous studies have shown that the microstructure of cement paste is finer and denser with the inclusion of graphene oxide sheets, resulting in an enhancement of its strength and durability[4].

Water permeability of graphene nanoengineered concrete

To gain further understanding into the durability of concrete and in particular whether graphene reinforcement plays any critical role in enhancing it, we have performed water permeability studies. In general, the durability of concrete depends on the capacity of a fluid to penetrate its microstructure. Degradation mechanisms of concrete often depend on whether water can penetrate into the concrete, possibly causing damage. To investigate the water permeability, we compared the water penetration in samples made of standard and IG reinforced concrete using the same IG concentrations to those presented in Fig. 5. The samples were cured for 7 days, fully dried and immersed in water up to the level as schematically shown in Fig. 6A. The black lines in Fig 6A show the level to which the water has infiltrated through the concrete structure after 7 days of immersion in water. It is evident that water penetrates to a lower level in the concrete reinforced with graphene than in standard concrete. Furthermore the length over which water infiltrates decreases with increasing the concentration of graphene, as apparent in Fig 6A. This effect is also visible in Fig 6B which plots the maximum distance (κ) between the initial water level and the infiltration level as a function of graphene concentration. Thus concrete reinforced with graphene acts as a barrier against water infiltration. In particular, a concentration of 0.8g/L of graphene decreases water permeability of concrete by up to ∼400%. These findings suggest that the enhanced formation of nucleation sites for the C-S-H hydration crystals and the high surface of graphene form a denser network of interlocked cement crystals which not only increases the mechanical properties of concrete but also acts as a water infiltration barrier and drastically decrease the amount of water that can penetrate the concrete matrix through capillary pores or crack voids. This property is extremely important for the long durability of concrete and in particular for the prevention of alkali-silica reaction (ASR), a swelling reaction that occurs in the presence of moisture between the highly alkaline cement paste and the reactive amorphous silica, resulting in serious cracking and critical structural problems. Indeed ASR can be prevented by a watertight graphene reinforced concrete barrier which could stop the evolution of the reaction[21].

Electrical and thermal properties of graphene nanoengineered concrete

The decreased water permeability of concrete reinforced with graphene could have profound consequences on its electric properties. Indeed, resistivity measurement is a common test for identifying damp in concrete structures, which typically show enhanced electrical conductivity in the presence of moisture infiltration. To quantify the effects of the addition of graphene to the cement and concrete on their electric properties, we have measured the resistivity and the temperature profile of several cement mixtures, with IG concentrations ranging from 0 (as reference) to 8 g/L, upon application of electric bias. The cement was moulded into a 4x4x15 cm bar mould and the concrete into a 10x10x10 cube moulds. Fig. 7 A and B show the measurement configuration for four-probes resistivity measurement and resistive heating measurements respectively. For the four probes measurements, the samples are biased using the outer electrodes with a source-measurement unit that also measures the current, as schematically shown in Fig. 7 A. The inter-electrode distance (l_{2p}) is 12 cm and 7 cm for the cement bars and concrete cubes, respectively. While biasing the sample, the potential difference between the two inner electrodes (V_{4p}) is measured using a voltmeter. Using the known inter-electrode distance for the inner electrodes (l_{4p}), the sample's resistivity (ρ) is given by $\rho = (A \cdot V_{4p}) / (I \cdot l_{4p})$, where I is the measured current. The total sample resistance (R) can then be calculated from $R = \rho \cdot l_{2p}/A$, whereas the contact resistance (R_c) can be estimated from $R_c = (V_A/I - R)/2$, where V_A is the applied bias. The results of the I-V sweeps, shown in Fig. 7 C, give the first indication of an increased resistivity with increased concentration of IG. The curves are plotted for concentrations of 0 to 1 g/L IG, with increasing concentration marked by the direction of the arrow, and show a steadily decreasing slope which suggests that the overall resistance in the circuit ($R_t = 2R_c + R$) is monotonously rising with the IG concentration. However, due to the nature of the conduction mechanism in concrete, which is predominantly governed by ionic drift, the slope of the I-V curve as well as the hysteresis around 0 V are dependent on the sweep rate. To exclude the time-dependent contribution, we have measured the steady-state resistivity by allowing the system to reach a constant cur-

rent over a period of 10 minutes. The measured currents and potential drops over the last 60 seconds were then averaged and used to determine the samples' resistivity, which is shown in Fig. 7 D. In contrast to the I-V sweeps, the steady-state resistivity shows an increase in resistivity that saturates under 3 kΩ-cm. The increase in resistivity suggests a hindering effect that could be caused by graphene which prevents water ingress. This, in turn, means that the compound is depleted of ions that are responsible for drift current, resulting in a diminished conductivity. It is important to note, however, that the estimated contact resistance remains relatively constant for the different concentrations and ranges between 10 and 50 Ω for the different samples, without showing a clear trend.

The relatively low resistivity of the graphene-reinforced concrete suggests that it can be readily utilised as a resistive heater for various applications. It is well known that resistive (Joule) heating occurs when a current is passed through a resistor and that the output heat (W) is given by $W = IV = V^2/R$, where V is the applied bias, I is the induced current and R is the resistance. However, since the difference in resistance between standard concrete and graphene reinforced concrete is relatively small, as suggested by the I-V sweeps in Fig. 7 E, it is expected that the power output of a standard cube will be relatively similar to that of a reinforced one. To maximise the power output, the cubes were biased using the inner electrodes, resulting in a lower resistance, for long periods of time, while the temperature was monitored continuously using an embedded thermocouple positioned half way between the inner electrodes. The surface temperature of the cubes was monitored periodically using a thermal camera. Fig. 7 F shows a graphene reinforced cube with an IG concentration of 8 g/L after it has been biased for 3 hours at 50 V on the left, and a reference unbiased cube at room temperature on the right. The striking difference in the thermal properties of the different concrete cubes is revealed when examining the heating (Fig. 7 G) and cooling (Fig. 7 H) rates of the cubes. The measurements show that both cubes follow a Newtonian cooling cycle: $dT/dt = k(T - T_0)$ where T is the instantaneous temperature, T_0 is the final (room) temperature, t is the time and k is a constant that depends on the thermal conductivity and heat capacity of the sample, as well as on the sample geometry. The Newtonian cooling cycle indicates that the emission of heat from the sample is dominated by conduction to the surrounding environment (as opposed to convection) which is the same mechanism by which the samples heat up. While the samples reach the same steady-state temperature over long periods of time, it is clear that the heating and cooling rate of the graphene reinforced cube is substantially lower than that of standard concrete. As discussed before, the lower temperature change rate can be a consequence of lower thermal conductivity, higher heat capacity, or a combination of both. However, the thermal imaging reveals that the spatial heat profile that develops across the surface of the two cubes is qualitatively similar, suggesting that the addition of graphene contributes to the concrete's thermal stability mainly through the increase in heat capacity.

The observed resistivity of graphene reinforced concrete is also crucial for preventing corrosion when steel rebars are used as conventional reinforcement. This potential corrosion of steel, which is an electrochemical process forming corrosion cells, causes deterioration of steel reinforced concrete beams or columns through expansion, cracking, and eventual spalling of the steel rebars' cover[22]. This decreases the bond strength between steel and concrete , thus leading to several damage to the overall structure. This incidence of damage is especially large in the structures exposed to deicing chemicals[22]. However, due to its resistive heater behaviour graphene reinforced concrete can exclude the addition of such chemicals and yet keep the corrosion formation to minimum in cases when steel embedding is required.

DISCUSSION

Previous studies[4–6,30–32] on nanoengineering cement through the incorporation of nanomaterials such as CNTs, GO, hBN and graphite have shown improvements on the strength and thermal properties. However the conventional approach to disperse nanomaterials in the dry cement matrix powder is costly, involves complex procedures, difficult to scale-up, and can lead to degradation of the mechanical properties of concrete. Progress on reinforcing cement materials with CNT is largely hampered by their chemical incompatibility with cement hydrates[23,24]. Likewise, while promising advancements have been made on GO-cement nanocomposites[4], GO reinforcement of concrete still poses major challenges. For example, GO is hydrophilic enough to absorb most of the water contained in the cement mortar and it has been shown to hamper the proper hydration of the cement, making dispersion of the GO within the matrix difficult. The multiple steps and additives linked to the oxidation change the molecular structure of GO sheets and can introduce defects, resulting in further uncertainties in the GO–cement molecular interactions. The cost-ineffectiveness of the method[4] used for the preparation of GO–cement nanocomposites, turns the production of GO–cement into a non-viable method for industrial scale production. Finally, most of the previous studies were performed on small samples of GO–cement composites that can not be directly applied to concrete, as the addition of sand and aggregate changes the physico-mechanical behaviour of the material.

The results presented here indicate that nanoengineering concrete through reinforcement with graphene leads to concrete composites with ultrahigh strength and at the same time it widens the range of functionalities. These materials will be of particular interest for the construction industry to develop new competitive structural applications. Besides enhancing the mechanical

performance, we demonstrate that the novel graphene-concrete composites satisfy multiple uses, with the added functionalities derived from the intrinsic properties of graphene. Thus, we show that graphene-concrete composites act as a barrier against water infiltration, which is an extremely desired property for long durability of concrete structures. Also, we demonstrate enhanced thermal stability mainly through the increase in heat capacity of concrete by incorporation of graphene. Finally, we show another proof of the existing nanomodification of cement crystals via X-Ray Diffraction data (See S11 in S.M.).

More importantly, it is evident that graphene reinforced concrete will have positive impact on the environment. Firstly, when compared to other reinforcement methods such as carbon nanotubes and graphene oxide, our method of production and final product are non-hazardous. This, along with the decreasing price of graphene, due to its continuous production scaling up would allow the direct fabrication and incorporation of graphene reinforced concrete in the construction industry. Another way in which graphene reinforced concrete will have a positive impact on the environment is by contributing to the decrease of carbon emissions due to cement manufacturing. Specifically, the production of concrete accounts for up to 7% of the global CO_2 emissions[25]. We estimate that reducing the quantity of cement by 50% of the required concrete material while still fulfilling the specifications for the loading of buildings, would lead to a significant reduction of 446kg/tonne of the carbon emissions by the cement manufacturing (see S10 in S.M.). These considerations make our graphene reinforced concrete a promising material for a better, more environmentally friendly construction industry.

MATERIALS AND METHODS

Liquid exfoliation of graphene: Various initial amounts of graphite flakes and surfactant sodium cholate (both supplied by Sigma Aldrich) were exfoliated using Silverson L5M shear mixer for 2h at 5000 rpm. Same exfoliation speed and time were used for the industrial grade 3 graphene nanoplatelets (supplied by cheaptubes.com). Both materials were mixed in a beaker using tap water.

Raman Measurements: Raman spectra were collected in a Renishaw spectrometer with a excitation laser wavelength of 532 nm, focused to a spot size of 1 μm diameter and x50 objective lens.

SEM Measurements: SEM micro-graphs were collected with a Phillips SEM. An acceleration voltage of 10kV, magnification of x20,000 and beam current of 0.13 nA was used.

Cubes preparation and testing: To prepare the concrete cube samples, Ordinary Portland Cement Type II, Fine dry sand and 10 mm coarse aggregate were used with ratio of 1:2:3 respectively. The water/cement ratio for all batches was kept the same – 0.57. Mixing time of the concrete batch was 10mins and the moulds were shaken for 6mins using standard vibrating machine. The cubes were demoulded 24h after preparation and were taken out of the water tank 24h prior to testing. The tests were performed using standard compressive loading apparatus supplied by Controls Group, with constant loading on specimens of 1000 N/s.

Beams preparation and testing: To prepare the concrete beams, Ordinary Portland Cement Type II, Fine dry sand and 10 mm coarse aggregate were used with ratio of 1:2:3 respectively. The water/cement ratio for all batches was kept the same – 0.5. Mixing time of the concrete batch was 10mins and the moulds were shaken for 6mins using standard vibrating machine. The beams were demoulded 24h after preparation and were taken out of the water tank 24h prior to testing. The tests were performed using standard 3 point bending apparatus supplied by Controls Group, with constant loading on specimens of 100 N/s.

Characterization of cement and concrete resistivity: Cement bars and concrete cubes were prepared in a mould to test the material's resistivity. The cement mixture was prepared in a similar way to the mixture used for mechanical testing, with varying concentration of IG in the water, ranging from 0 (reference) to 8 g/L. The cement bars were 15 cm long with a cross section area of 4×4 cm, whereas the concrete cubes were 10×10×10 cm. After the cast has hardened, the samples were cured in water at 40°C for seven days and allowed to dry for a day in ambient conditions prior to their measurements. To facilitate the electric characterisation, four copper mesh electrodes were embedded in each cast keeping a distance of 7 and 4 cm between the inner electrodes, and 12 and 7 cm between the outer electrodes of the bars and cubes, respectively. For each mould, the area of the electrodes was one centimetre smaller in width and height than the cross section of the mould to allow the electrodes to be fully embedded without protruding through the surface. The top part of the copper mesh was kept longer to allow for electric connections. To measure resistivity, the outer electrodes were voltage biased between -20 and +20 V, with the current measured over 10 minutes to allow for the system to stabilise. The potential drop between to two inner electrodes was monitored by a voltmeter.

Heating and cooling of concrete: In some of the cement bars and concrete cubes, a K-type thermocouple was embedded in equal distance between the two inner electrodes. The inner electrodes were then biased using a power generator outputting up to 40 W of power over several hours while the thermocouple was monitored constantly. Thermal images were acquired using a FLIR infrared camera.

SUPPLEMENTARY MATERIALS Supplementary material for this article, including detailed materials and methods, is available.

S1.Liquid exfoliation of Graphene
S2.Transfer method from the liquid to the substrate
S3.SEM analysis

REFERENCES AND NOTES

* E-mail: m.f.craciun@exeter.ac.uk

[1] F.M. Lea, The Chemistry of Cement and Concrete, 1970.
[2] J. Lee S. Mahendra, P. J. J. Alvarez, ACS Nano 2010, 7, 4.
[3] N. Silvestre, J. de Brito, European Journal of Environmental and Civil Engineering 2015, 20, 4.
[4] Z. Pan, L. He, L. Qiu, A. Korayem, G. Li, J. W. Zhu, F. Collins, D. Li, W. H. Duan, Cement & Concrete Composites 2015, 58, 140-147.
[5] E. Horszczaruk, E. Mijowska, R. J. Kalenczuk, M. Aleksandrzak, S. Mijowska, Cement & Concrete Composites 2015, 78, 1.
[6] A. Sedaghat, M. K. Ram, A. Zayed, R. Kamal, N. Shanahan, Open Journal of Composite Materials 2014, 4, 1.
[7] S. Chuah, Z. Pan, J. G. Sanjayan, C. M. Wang, W. H. Duan, Construction and Building Materials 2014, 73 113124.
[8] T. Bointon, M. Barnes, S. Russo, M. F. Craciun, Advanced Materials 2015, 28, 4200-4206.
[9] S. Lee, S. H. Eom, J. S. Chung, S. . Hur, Chemical Engineering Journal 2013, 233, 297-304.
[10] M. Lotya, Y. Hernandez, P. J. King, R. J. Smith, V. Nicolosi, L. S. Karlsson, F. M. Blighe, S. De, Z. Wang, I. T. McGovern, G. S. Duesberg and J. N. Coleman, J. Am. Chem. Soc. 2009, 131, 36113620.
[11] M. Lotya, P. J. King, U. Khan, S. De, J. N. Coleman, ACS Nano 2010, 6, 3155-3162.
[12] K. R. Paton, E. Varrla, C. Backes, R. J. Smith, U. Khan, A. ONeill, C. Boland, M. Lotya, O. M. Istrate, P. King, T. Higgins, S. Barwich, P. May, P. Puczkarski, I. Ahmed, M. Moebius, H. Pettersson, E. Long, J. Coelho, S. E. OBrien, E. K. McGuire, B. M. Sanchez, G. S. Duesberg, N. McEvoy, T. J. Pennycook, C. Downing, A. Crossley, V. Nicolosi, J. N. Coleman, Nature Materials 2014, 13, 624-630.
[13] W. Liu, B. Xia, X. Wang, J. Wang, Frontiers of Material Science 2012, 6, 176-182.
[14] A. Eckmann, A. Felten, A. Mishchenko, L. Britnell, R. Krupke, K. S. Novoselov, C. Casiraghi, Nano Letters 2012, 12, 3925-3930.
[15] X. Gu, Basic Properties of Concrete Structures , Springer Berlin Heidelberg, 2016.
[16] I.G. Richardson, Cement and Concrete Research 2008, 38, 137 - 158.
[17] J. Lee, D. Yoon, H. Cheong, NANO letters 2012, 12, 4444-4448.
[18] F. Babak, H. Abolfazi, G. Parviz, The Scientific World Journal 2014, 276323.
[19] T. Tanabe, K. Sakata, H. Mihashi, R. Sato, K. Maekawa, H. Nakamura, Creep Shrinkage and Durability Mechanics of Concrete and Concrete Structures, Taylor and Francis is Group, 2009.
[20] J.B. Mander, M.J.N. Priestley, and R.Park, J. Structural Engineering 1988, 114(8): 1804-1826
[21] N. B. Winter, Understanding Cement: An Introduction to Cement Production, Cement Hydration and Deleterious Processes in Concrete, Microanalysis Consultants, 2012.
[22] P. Kumar Mehta, P. J. M. Monteiro, Concrete: Microstructure, Properties, and Materials, Prentice-Hall, Inc., 1993 **p.165**.
[23] Y Saez de Ibarra, J. J. Gaitero, E. Erkizia, I. Campillo, Physica Status Solidi A-Applications and Materials Science 2006, 203, 6.
[24] M. Konsta-Gdoutos, Z. Metaxa, S. P. Shah, Cement & Concrete Composites 2010, 40, 7.
[25] WBCSD. *CSI Progress report* (June 2012).
[26] D. Johnson, B. P. Dobson and K.S. Coleman, Current Opinion in Colloid & Interface Science 2015, 20, 367-382.
[27] K. Erickson, R. Emi, Z. Lee, N. Alem, W. Gannett and A. Zettl, Advanced Materials 2010, 22, 4467-4472.
[28] I.G. Richardson, Cement and Concrete Research, 2008, 38, 137 158.
[29] Paul E. Stutzman, Pan Feng and Jeffrey W. Bullard, Journal of Research of the National Institute of Standards and Technology 2016, 121.
[30] Mohammad A. Rafiee, Tharangattu N. Narayanan, Daniel P. Hashim, Navid Sakhavand, Rouzbeh Shahsavari, Robert Vajtai, Pulickel M. Ajayan, Advanced Functional Materials, 2013, 23, 5624-5630.
[31] Fakhim Babak,1 Hassani Abolfazl, Rashidi Alimorad and Ghodousi Parviz, The Scientific World Journal, 2014, 2014.
[32] M.L. Cao, H.X. Zhang, C. Zhang,Journal of Central South University. 23 (2016) 919925.

Acknowledgments General: we acknowledge Ian Moon, Siobhan Kelly, Julian Yates and Roger Perrett for the technical support in the concrete laboratories. DD acknowledges fruitful discussions with Lachlan Marnham.
Funding: we acknowledge financial support from EPSRC (Grant EP/J000396/1, EP/K017160, EP/K010050/1, EP/G036101/1, EP/M002438/1, EP/M001024/1), from the Royal Society Travel Exchange Grants 2012 and 2013, from the European Commission (H2020-MSC-IF-2015-704963 and H2020-MSC-IF-2015-701704) and from the Royal Academy of Engineering.
Author contributions: D.D conceived the project, designed the experiments, prepared and tested the water dispersed graphene and all of the various concrete structures investigated. I.A performed the measurements and analysis of the electrical and thermal properties of cement and concrete samples, took and analysed the

SEM micrographs. N.J.T. contributed to the design of the electrical and thermal characterisation experiments and to the analysis of conductive cement and concrete samples O.G. prepared and tested cube samples for cycle-loading analysis, A.I.S.N. contributed to the preparation of water dispersed graphene, prepared figures for the supplementary material and contributed to the discussion. M.D.B. contributed to the analysis of the Raman measurement. F.W. contributed to water permeability study. S.R. and M.F.C. directed and supervised the project. D.D and M.F.C wrote the paper with input from all authors.

Competing interests: The authors declare that they have no competing financial interests.

Data and materials availability: All data needed to evaluate the conclusions in the paper are present in the paper and/or the Supplementary Materials. Additional data related to this paper may be requested from the authors.

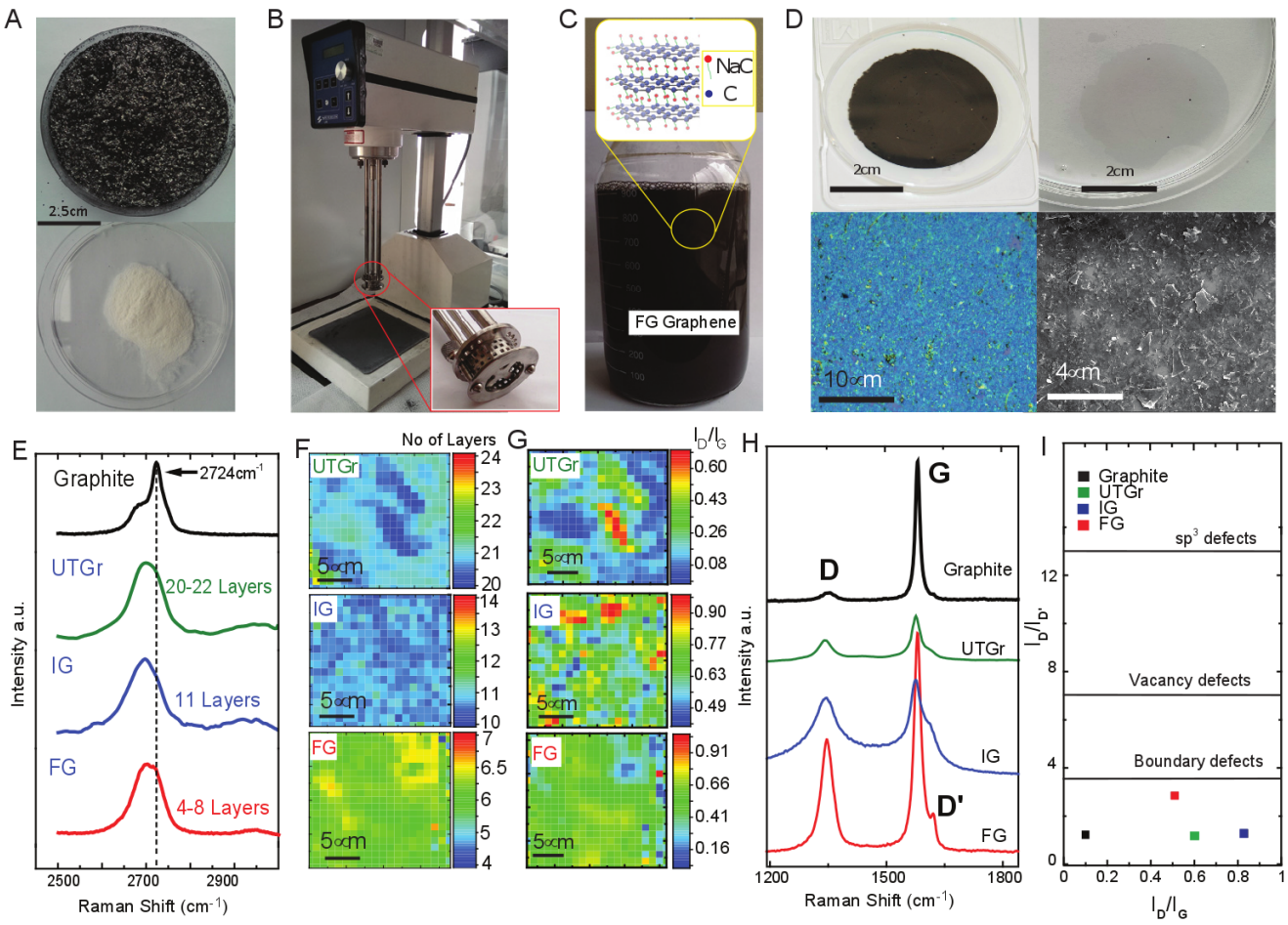

FIG. 1. **Fabrication and characterization of graphene.** (**A**) Photograph of graphite flakes and of surfactant sodium cholate used for production of water dispersed functionalised graphene. (**B**) Photograph of Silverson L5M laboratory mixer used to obtain the graphene solutions. The inset shows the rotor head of the mixer, with diameter of the head 32 mm, square holes. (**C**) Photograph of typical surfactant-stabilised graphene solution. The inset is a schematic of the graphene layers functionalised with the surfactant molecules. (**D**) Photographs of membrane with 0.025 μm filter with deposited surfactant-stabilised graphene dispersions (top left), of continuous graphene film floating on water surface (top right). The bottom panels show optical (left) and scanning electron microscopy (right) images of the graphene film deposited on Si/SiO_2 substrate. (**E**) Comparison of the 2D peak position of graphite and different thicknesses of graphene flakes. (**F**) Raman map of the number of layers across the continuous film. (**G**) Maps showing the I_D/I_G ratios of a uniform area of the continuous graphene film for each of the three types deposited on SiO_2 substrates. (**H**) One spectrum of each graphene type showing the G, D and D$\prime$ peaks in comparison with bulk graphite. (**I**) Plot of the $I_D/I_{D'}$ ratios corresponding to the four I_D/I_G ratios from H showing that there are no defects introduced to the basal plane of the graphene dispersions.

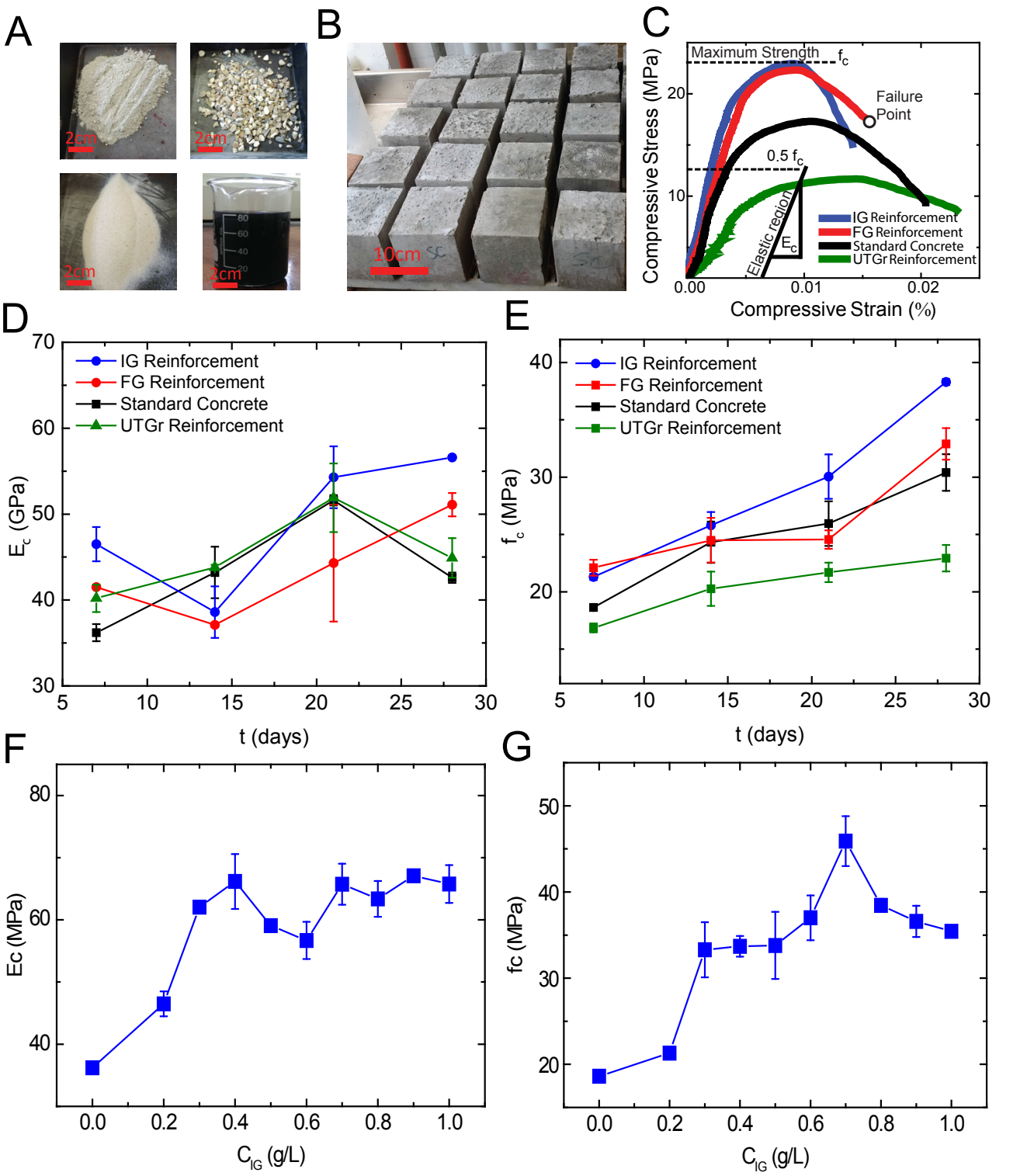

FIG. 2. **Compressive strength of graphene reinforced concrete.** (**A**) Materials used for concrete preparation and sample of graphene solution. (**B**) Concrete samples used for testing. (**C**) Typical stress–strain curve of concrete cube measured under compressive loading, comparing the standard concrete with graphene (IG and FG) and graphite (UTGr) reinforcements. (**D**) The evolution of Young's modulus (E_c) over time (t) for standard concrete and concrete reinforced with graphene (IG and FG) and graphite (UTGr). (**E**) The evolution of concrete compressive strength (f_c), over time (t) for standard concrete and concrete reinforced with graphene (IG and FG) and graphite (UTGr). (**F**) Investigation of early age E_c of concrete (after 7 days of curing) for increasing graphene concentration and (**G**) early age f_c. Each data point is an average of 3 cubes.

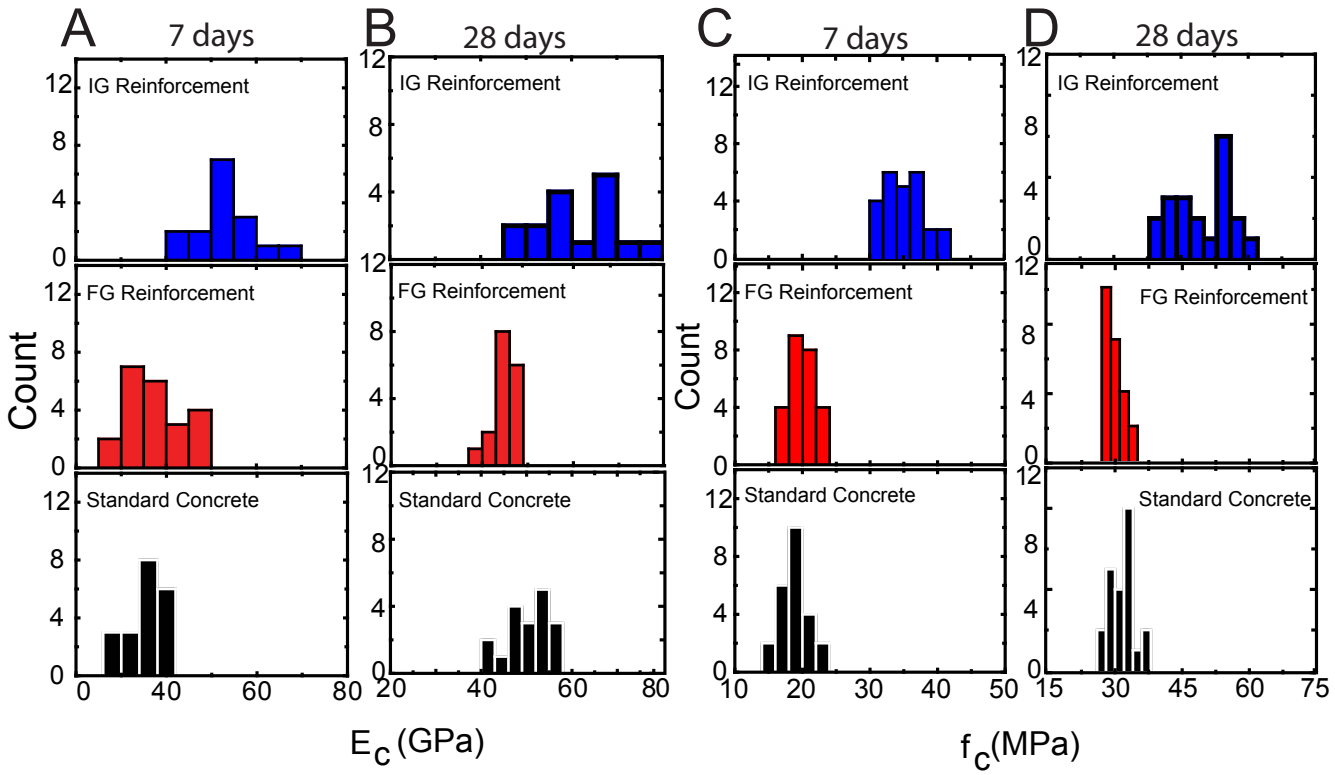

FIG. 3. **Statistical study of compressive strength of graphene reinforced concrete.** (**A**) Statistical study on Young's modulus of the material (E_c) after 7 days and (**B**) after 28 days of 0.7g/L IG, FG and standard concrete experimental groups. (**C**) The same statistical study of the compressive strength (f_c) after 7 days and (**D**) after 28 days.

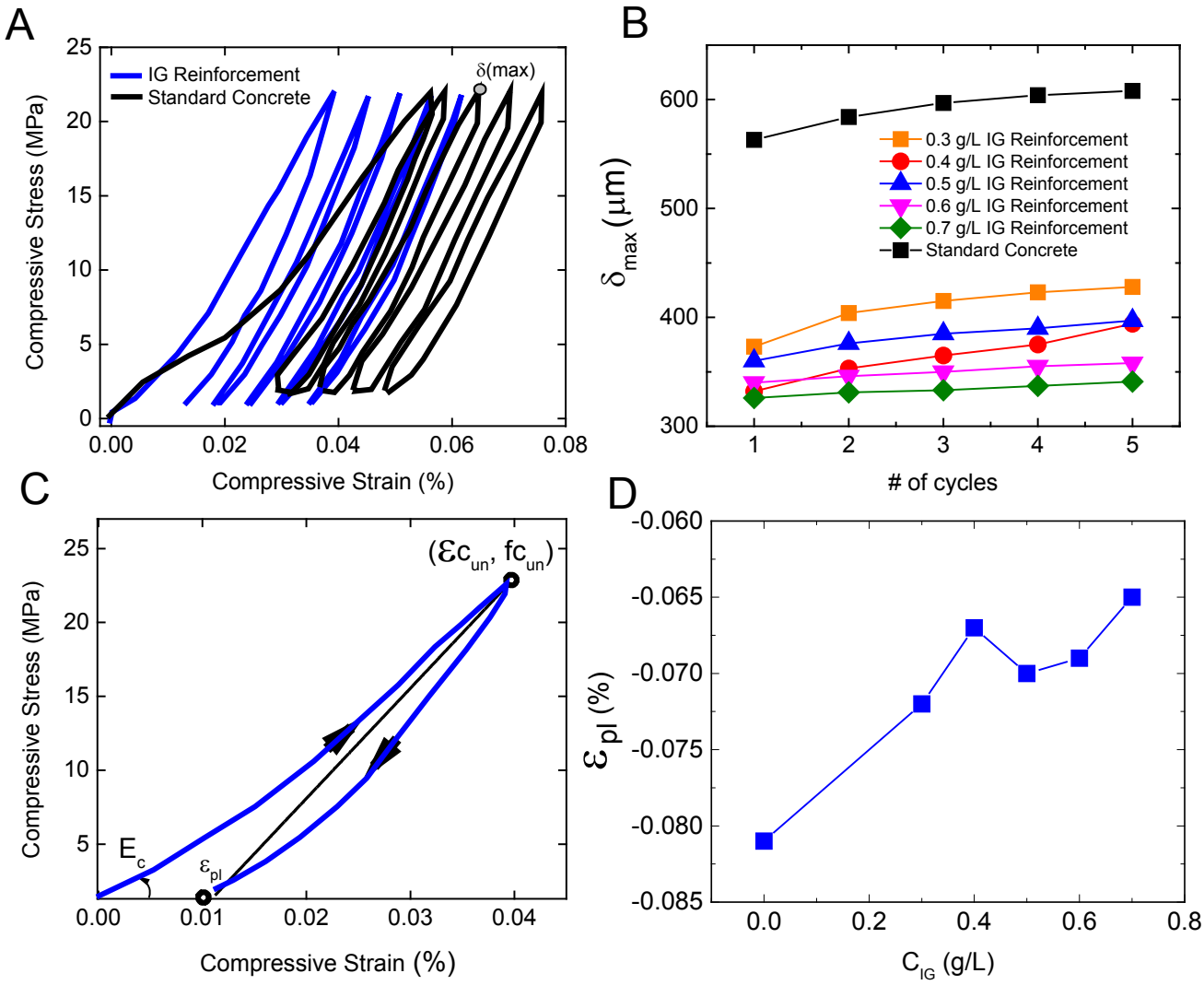

FIG. 4. **Cycling loading compressive tests of graphene reinforced concrete.** (**A**) Measurement showing typical stress-strain relationship of cycling loading compressive tests on a concrete cube. The loops have been spaced out by $\Delta(100\mu\text{m})$ for better reading and the maximum displacement (δ_{max}) of each loop has been highlighted in red. (**B**) Comparison of the maximum displacement under compressive cycling loading for reinforced cubes with increasing graphene concentration. (**C**) The first loop of the cyclic loading measurement is extracted to study the unloading curve. The maximum plastic strain is calculated from the secant line of the unloading curve. (**D**) The evolution of the plastic strain as a function of increased graphene concentration in the reinforced concrete samples.

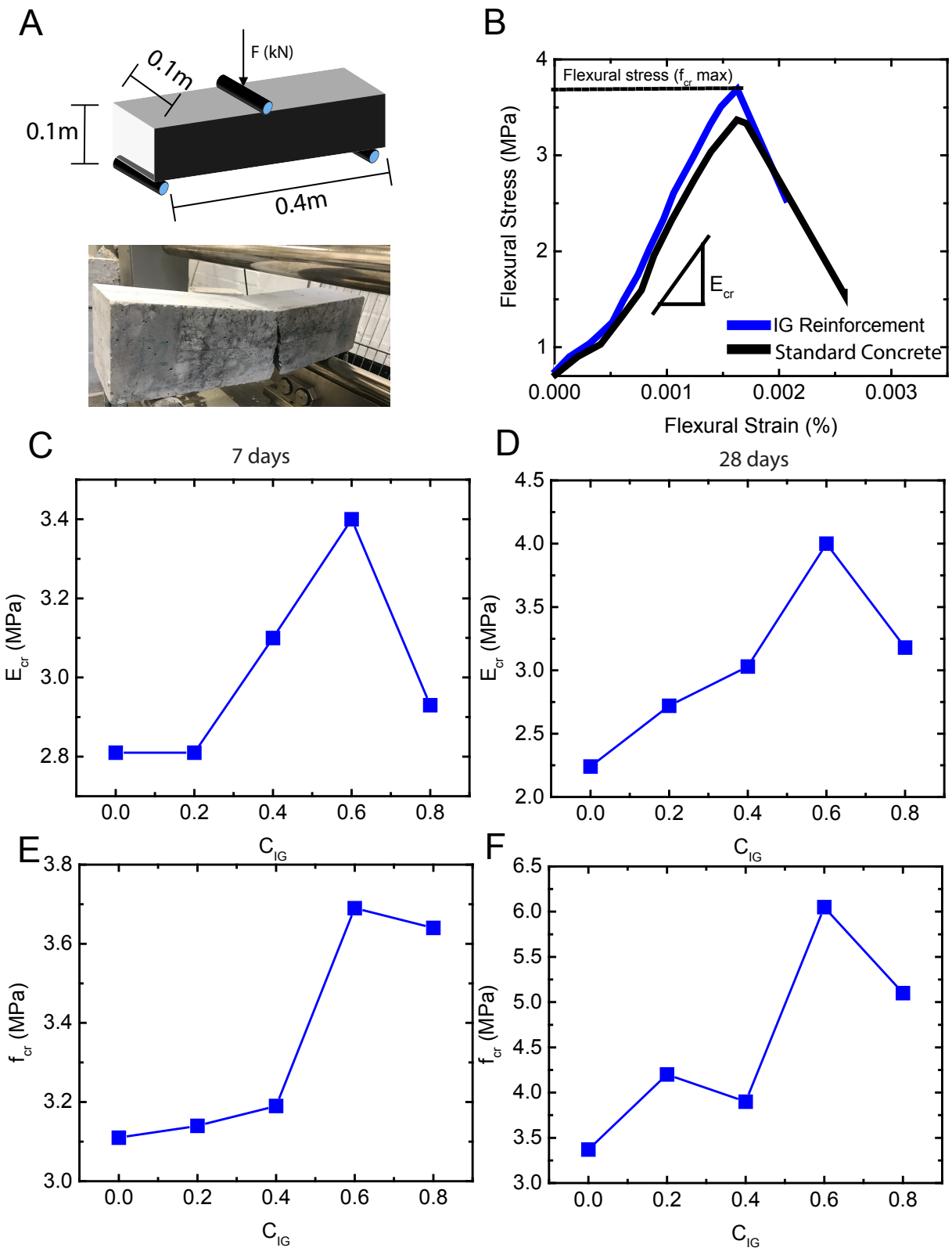

FIG. 5. **Flexural strength of graphene reinforced concrete.** (**A**) Top: Schematic showing a typical 3-point bending test for measuring the flexural properties of a concrete beam. Bottom: photograph of the actual concrete beam after failure. (**B**) Typical stress-strain curve under flexural loading showing the maximum flexural stress and strain f_{cr} of both the standard concrete and the graphene reinforced one (IG). (**C**) Evolution of early age flexural modulus (E_{cr}) with increasing graphene concentration C_{IG} in IG reinforced concrete. (**D**) Evolution of late age flexural modulus (E_{cr}) with increasing graphene concentration C_{IG} in IG reinforced concrete. (**E**) Evolution of early age flexural strength f_{cr} with increasing graphene concentration C_{IG} in IG reinforced concrete. (**F**) Evolution of late age flexural strength f_{cr} with increasing graphene concentration C_{IG} in IG reinforced concrete.

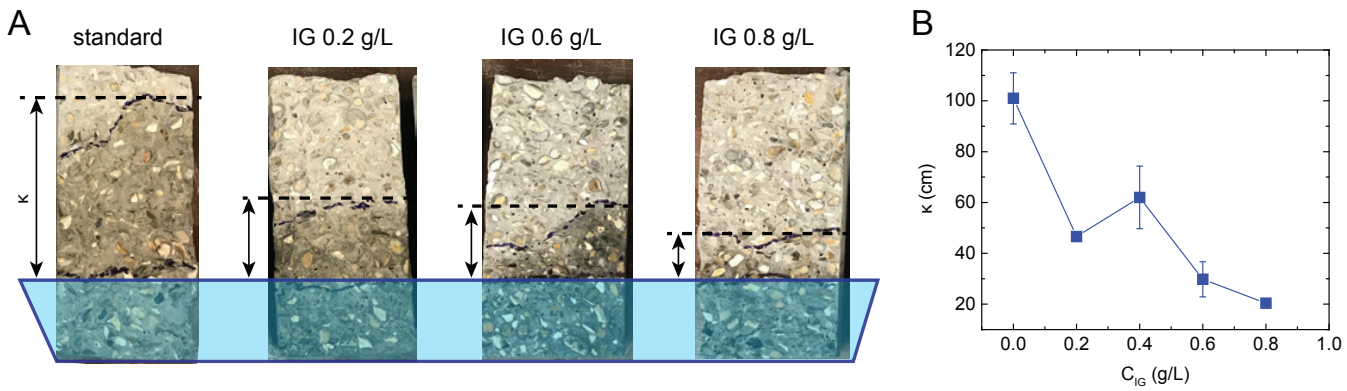

FIG. 6. **Water impermeability of graphene reinforced concrete.** (**A**) Photographs of concrete structures tested for permeability after 7 days in water. (**B**) The maximum depth of water penetration in the standard concrete and graphene reinforced (IG) concrete for the tested concrete structures.

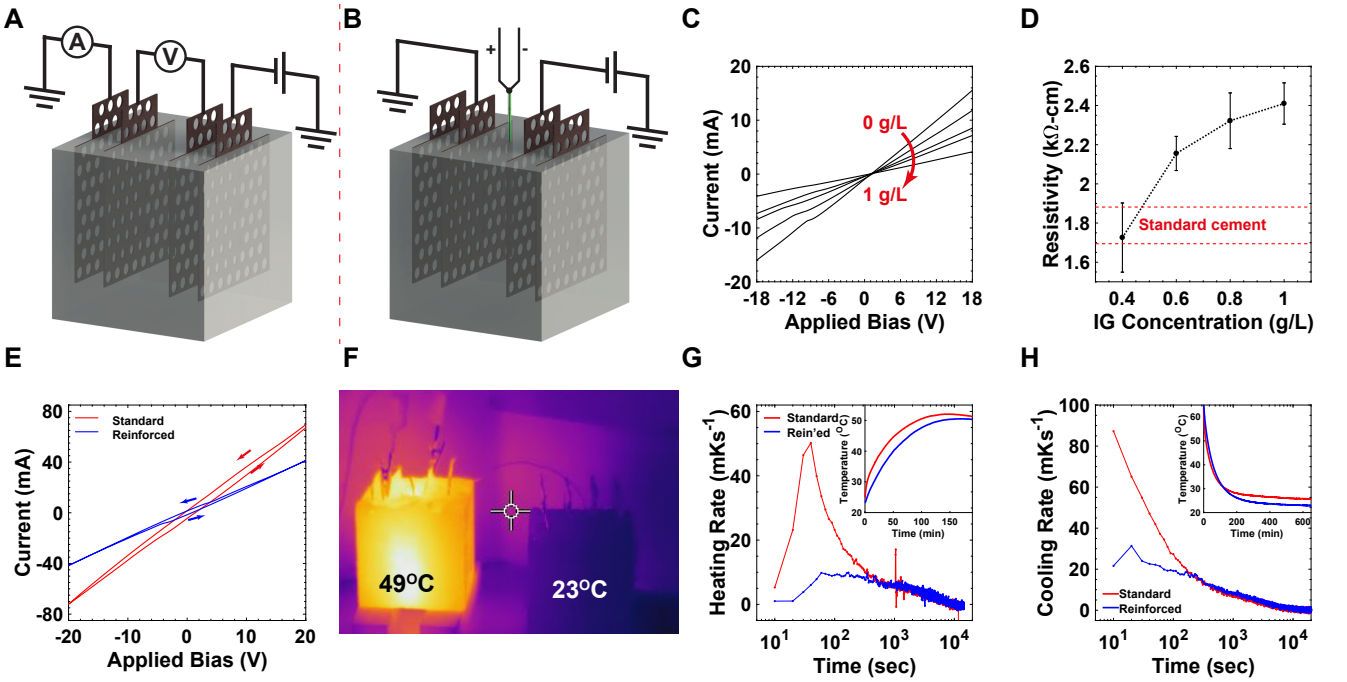

FIG. 7. **Electrical and thermal properties of graphene reinforced concrete.** (**A**) Schematic illustration of a concrete cube showing the embedded electrodes (not to scale) and the electric 4-probe configuration used to measure the resistivity. (**B**) The electric configuration used to heat up the cubes and measure the developing temperature profile. (**C**) Current-Voltage (I-V) curves measured on cement bars with various concentration of IG ranging from 0 to 1 g/L. The arrow shows the direction of increasing IG concentration. (**D**) Equilibrium resistivity measured on cement bars with IG concentration ranging from 0.4 to 1 g/L. The red dashes show the resistivity obtained in standard cement. (**E**) I-V sweeps of standard concrete (red) and graphene reinforced concrete (blue) using 8 g/L IG concentration. (**F**) Thermal image of graphene reinforced concrete cube biased with 50 V over three hours (left), and a reference unbiased cube (right). (**G**) Heating rate of standard (red) and graphene reinforced (blue) concrete cubes shown on a semi-logarithmic scale for clarity. The inset shows the heating curves for both samples.(**H**) Cooling rate of standard and graphene reinforced concrete cubes, shown on a semi-logarithmic scale using the same colour convention from (G). The inset shows the cooling curves obtained for both samples.